Deterministic Hadamard gate for microwave cat-state qubits in circuit QED

Simon E. Nigg*

Department of Physics, University of Basel, Klingelbergstrasse 82, CH-4056 Basel, Switzerland

(Received 27 January 2014; published 27 February 2014)

We propose the implementation of a deterministic Hadamard gate for logical photonic qubits encoded in superpositions of coherent states of a harmonic oscillator. The proposed scheme builds on a recently introduced set of conditional operations in the strong dispersive regime of circuit QED [Z. Leghtas *et al.*, Phys. Rev. A **87**, 042315 (2013)]. We further propose an architecture for coupling two such logical qubits and provide a universal set of deterministic quantum gates. Based on parameter values taken from the current state of the art, we give estimates for the achievable gate fidelities accounting for fundamental gate imperfections and finite coherence time due to photon loss.

DOI: 10.1103/PhysRevA.89.022340 PACS number(s): 03.67.Lx, 42.50.Dv, 42.50.Pq, 85.25.−j

I. INTRODUCTION

While digital (discrete) information encoding is classically advantageous over analog (continuous) information encoding, this is no longer true in the quantum case. Indeed, even when information is encoded into eigenstates of operators with a discrete spectrum, the principle of superposition allows for a continuum of errors. This has been recognized early on and it was shown that continuous variable quantum computation is theoretically as powerful as discrete variable quantum computation [1]. Encoding an effective two-level system into the large Hilbert space of a continuous variable system, such as that of a harmonic oscillator, may even be more advantageous by allowing for more compact information processing and error correction schemes [2].

The last decade has witnessed steady improvements in coherence times of quantum superconducting circuits [3,4], as well as significant advances in quantum coherent frequency conversion between the optical and microwave frequency ranges [5]. These developments have revived interest in the possibility, originally proposed in the context of linear optics [6], of encoding information in superpositions of coherent states of light known as cat states [7–9], in reference to Schrödinger's famous thought experiment [10]. The linear scaling of the decoherence rate with the size of such states, in this case the average number of photons, is an obvious drawback of such a scheme. However, recently a proposal for encoding, manipulating, and protecting information in photon number parity eigenstates of microwaves dispersively coupled to a superconducting qubit has been put forward [11,12]. This provides an exciting new development in the field of coherent state quantum computing.

In this work we follow an alternative route to implement a universal set of quantum gates for coherent state qubits. In particular we provide a fully deterministic Hadamard gate, the fidelity of which is characterized for realistic parameters by solving the Lindblad master equation numerically, accounting for the effects of photon loss in the dispersive coupling regime. Probabilistic Hadamard gates for coherent state qubits have been proposed in the linear optics regime in Refs. [6,13–15] and implemented in Ref. [16].

*simon.nigg@unibas.ch

II. SYSTEM AND MODEL

The system we consider, called a 3D transmon [3], consists of a Josephson junction antenna, dipole coupled to the electric field of a microwave resonator as illustrated in Fig. 1. Approximating the nonlinear Josephson oscillator by a two-level system, consisting of its two lowest eigenstates $|g\rangle$ and $|e\rangle$, we model this system by the following Hamiltonian [17–19]

$$\boldsymbol{H}_0 = \omega_c \boldsymbol{a}^\dagger \boldsymbol{a} + \frac{\omega_{eg}}{2}\boldsymbol{\sigma}^z - \chi \boldsymbol{a}^\dagger \boldsymbol{a}\boldsymbol{\sigma}^z. \tag{1}$$

Here $\boldsymbol{a}$ annihilates a photon in the cavity mode with frequency ω_c and $\boldsymbol{\sigma}^z = |e\rangle\langle e| - |g\rangle\langle g|$ is a standard Pauli operator for the two-level system with transition frequency ω_{eg}. This model is valid in the dispersive (i.e., off-resonant) single-mode coupling regime $\chi/\Delta \ll 1$ and for photon numbers satisfying $n \ll n_{\rm crit} = \Delta/\chi$, with $\Delta = |\omega_c - \omega_{eg}|$. It is convenient to transform to a rotating frame via the transformation

$$\boldsymbol{U}(t) = \exp\left[-i\left(\frac{\omega_{eg}}{2}\boldsymbol{\sigma}^z + (\omega_c + \chi)\boldsymbol{a}^\dagger \boldsymbol{a}\right)t\right]. \tag{2}$$

From now on we thus consider the Hamiltonian in this rotating frame which reads

$$\boldsymbol{H}_0 = -2\chi \boldsymbol{a}^\dagger \boldsymbol{a}\,|e\rangle\langle e|\,. \tag{3}$$

In addition we shall consider the following (classical) drive terms for the cavity ($\boldsymbol{H}_{\rm c}$) and the qubit ($\boldsymbol{H}_{\rm q}$), which in the rotating frame read

$$\boldsymbol{H}_{\rm q}(t) = \sum_{j=1}^{N_0} \frac{\Omega_j(t)}{2}(e^{i(\Delta_{\rm qd}^{(j)}t+\delta_j)}\boldsymbol{\sigma}^- + \text{H.c.}) \tag{4}$$

$$\boldsymbol{H}_{\rm c}(t) = \sum_{j=1}^{N_0} \varepsilon_j(t)(e^{i(\Delta_{\rm cd}^{(j)}t+\mu_j)}\boldsymbol{a} + \text{H.c.}). \tag{5}$$

Here $\Delta_{\rm qd}^{(j)} = \nu_j - \omega_{eg}$ and $\Delta_{\rm cd}^{(j)} = \eta_j - \omega_c - \chi$, where Ω_j and ε_j are the drive strengths, ν_j and η_j the drive frequencies, and δ_j and μ_j the drive phases.

Starting from this model, it was proposed in Leghtas *et al.* [11] and demonstrated experimentally in Vlastakis *et al.* [20], how to deterministically prepare superpositions of coherent states of the cavity field, also known as cat states. This is made possible because although χ is small compared with the detuning between the cavity and the transmon, it is many orders of magnitude larger than the linewidths of the transmon

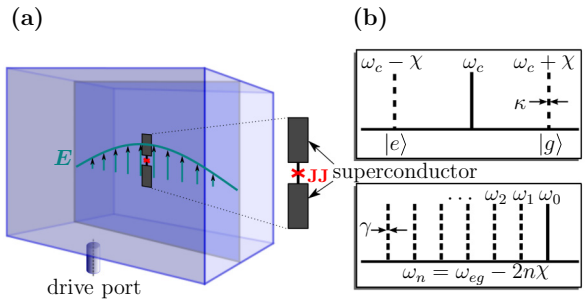

FIG. 1. (Color online) (a) A superconducting dipole antenna with a Josephson junction (JJ) at its center (transmon) is coupled to the quantized electric field $\boldsymbol{E}$ inside a three-dimensional microwave resonator. (b) Schematics of the spectra of the cavity (upper panel) and transmon (lower panel) in the strong dispersive regime.

and cavity resonances, respectively given by γ and κ [see Fig. 1(b)]. This spectral resolution enables selective rotations of the transmon conditioned on the number of photons in the cavity and selective displacement operations of the cavity field conditioned on the state of the transmon [11].

In this work we account for the effects of photon loss in the Lindblad master equation formalism. We shall assume that the transmon is T_1 limited, i.e., that the intrinsic dephasing rate $\gamma_\varphi = 0$ and that the relaxation rate is solely due to the Purcell effect [17,18], i.e., that $\gamma = (\chi/\Delta)\kappa$. The (zero-temperature) master equation for the density matrix thus takes the form [21]

$$\dot{\rho} = -i[\boldsymbol{H},\rho] + \kappa\mathcal{D}[\boldsymbol{a}]\rho + \gamma\mathcal{D}[\boldsymbol{\sigma}^-]\rho, \tag{6}$$

with $\mathcal{D}[\boldsymbol{A}]\rho = (2\boldsymbol{A}\rho\boldsymbol{A}^\dagger - \boldsymbol{A}^\dagger\boldsymbol{A}\rho - \rho\boldsymbol{A}^\dagger\boldsymbol{A})/2$ and $\boldsymbol{H} = \boldsymbol{H}_0 + \boldsymbol{H}_\mathrm{q} + \boldsymbol{H}_\mathrm{c}$. This equation is solved numerically using the PYTHON library QUTIP [22].

We follow the notation introduced in Ref. [11] and denote by $\boldsymbol{D}^j_\alpha$ a displacement of the cavity field by the amplitude α, conditioned on the transmon being in state $|j\rangle \in \{|g\rangle, |e\rangle\}$. Similarly, a rotation of the transmon by an angle θ around the axis $\hat{n}_\phi = \cos(\phi)\hat{x} + \sin(\phi)\hat{y}$, conditioned on there being n photons in the cavity is denoted with $\boldsymbol{X}^n_{\theta,\phi}$. Finally, $\boldsymbol{\Pi}^e$ denotes the photon number parity operator conditioned on the transmon being in the excited state $|e\rangle$. Ideally, these operations are given by

$$\boldsymbol{D}^j_\alpha = \exp(\alpha\boldsymbol{a}^\dagger - \alpha^*\boldsymbol{a}) \otimes |j\rangle\langle j| + \mathbb{1} \otimes |\bar{j}\rangle\langle\bar{j}| \tag{7}$$

$$\boldsymbol{X}^n_{\theta,\phi} = |n\rangle\langle n| \otimes e^{i\frac{\theta}{2}\hat{n}_\phi\cdot\vec{\boldsymbol{\sigma}}} + \textstyle\sum_{m\neq n}|m\rangle\langle m| \otimes \mathbb{1} \tag{8}$$

$$\boldsymbol{\Pi}^e = \exp(i\pi\boldsymbol{a}^\dagger\boldsymbol{a}) \otimes |e\rangle\langle e| + \mathbb{1} \otimes |g\rangle\langle g|, \tag{9}$$

where we used the notation $\bar{g} = e$, $\bar{e} = g$. Operations (7) and (8) can be realized by appropriately applying the drive terms $\boldsymbol{H}_\mathrm{q}$ and $\boldsymbol{H}_\mathrm{c}$ while operation (9) is realized by letting the dispersive term (3) act alone for a time $T_\pi = \pi/(2\chi)$ [11,20,23]. Pulse imperfections and nonorthogonality of coherent states with finite amplitudes result in small corrections as described in more details in the Supplemental Material of Ref. [20].

III. COHERENT STATE QUBITS

In binary quantum logic, the two computational states may be encoded in any two mutually orthogonal states. Even in the case of discrete variable quantum computation there thus exists a continuum of possible encodings. In the discrete variable case, the computational states are typically chosen to be the ground and the first excited states of the system representing the qubit. This choice is advantageous because these states are stationary, i.e., their time evolution is given by a (trivial) phase factor and relaxation provides a natural way to reset the qubit. Different types of encodings have been considered also for continuous variables and it has been shown theoretically that universal quantum computation is possible also in this case [1]. Of interest here is the continuous variable encoding of information in superpositions of coherent states of a harmonic oscillator, first proposed in Ralph *et al.* [6] and Gilchrist *et al.* [24] in the context of linear optics. Importantly, coherent states (with nonzero amplitude) are not eigenstates of the harmonic oscillator Hamiltonian $\boldsymbol{H}_\mathrm{osc} = \omega\boldsymbol{a}^\dagger\boldsymbol{a}$, but under the action of the latter their phase evolves periodically as $|\alpha(t)\rangle = \exp[-i\omega t\boldsymbol{a}^\dagger\boldsymbol{a}]\,|\alpha(0)\rangle = |e^{-i\omega t}\alpha(0)\rangle$; a property that is made use of in the implementation of the photon number parity gate $\boldsymbol{\Pi}^e$ given above. Coherent states are often described as classical states of light owing to the fact that they are steady-state solutions of the damped, classically driven, harmonic oscillator. The latter property lies at the heart of recent proposals to stabilize superpositions of coherent states—clearly nonclassical states of light—by engineering an appropriate dissipative environment [12,25]. Finally, two coherent states of finite amplitude are never truly orthogonal since $\langle\alpha|\beta\rangle = \exp[-(|\alpha|^2 + |\beta|^2 - \alpha^*\beta - \alpha\beta^*)/2]$.

Coherent states have interesting relaxation and coherence properties [26]. Being eigenstates of the photon annihilation operator, the loss of a photon at a rate κ leaves a coherent state in a coherent state with damped amplitude, i.e., $|\alpha\rangle \to |\alpha e^{-\frac{\kappa}{2}t}\rangle$. In particular this implies that the mean photon number $\bar{n}(t) = |\alpha(t)|^2$ of a coherent state decays at the single-photon loss rate κ independently of its amplitude. In this sense a coherent state is more robust against photon loss than a Fock state $|N\rangle$, the occupation of which decays at a rate $N\kappa$ [27,28]. However, a superposition of coherent states such as the even parity cat state $\mathcal{N}(|\alpha\rangle + |-\alpha\rangle)$, with normalization factor $\mathcal{N} = 1/\sqrt{2 + 2\exp(-2|\alpha|^2)}$, decoheres at the enhanced rate $2\bar{n}\kappa$ [at short times $t \ll 1/(\bar{n}\kappa)$]. The latter property makes it clear that quantum information processing with cat states will only succeed if fast and reliable quantum error correction can be done on such qubits. Recently encouraging results in this direction in both theory and experiment have been obtained [12,15,23,25,29].

In this work, we consider specifically the following two logical qubit encodings [6]

$$|0\rangle_L = |0\rangle, \quad |1\rangle_L = |\alpha\rangle \tag{10}$$

and [23]

$$|\mathcal{C}^+_\alpha\rangle = \mathcal{N}(|\alpha\rangle + |-\alpha\rangle), \quad |\mathcal{C}^+_{i\alpha}\rangle = \mathcal{N}(|i\alpha\rangle + |-i\alpha\rangle). \tag{11}$$

We shall further assume that $|\alpha|$ is sufficiently large such that $\langle 0|\alpha\rangle = \exp(-|\alpha|^2/2) \approx 0$ and $\mathcal{N} \approx 1/\sqrt{2}$ (for example, for $\alpha = 4$, one has $\langle 0|\alpha\rangle = 3.4 \times 10^{-4}$). The $\{|0\rangle_L, |1\rangle_L\}$ encoding, which we shall call the computational encoding, turns out to be more convenient for logical operations utilizing the dispersive interaction between the microwaves and the

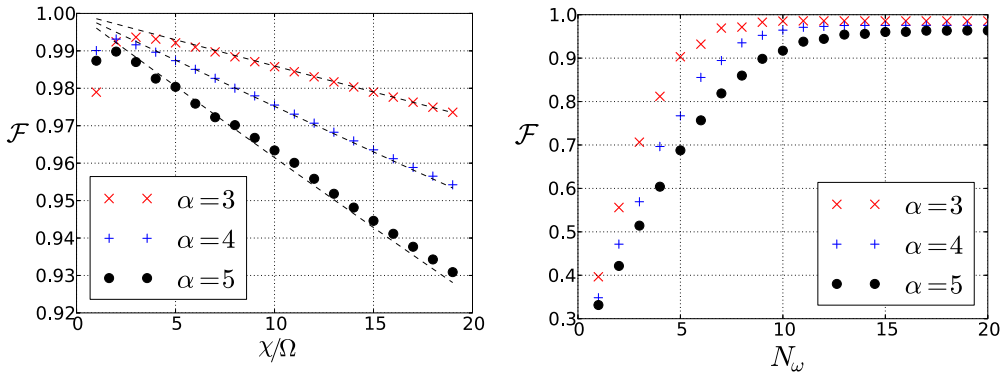

FIG. 2. (Color online) Fidelity of the photon number parity conditional π-pulse from the numerical solution of Eq. (6) with $\chi/(2\pi) = 50\,\mathrm{MHz}$, $\kappa = 10^{-4}\chi$. Left: Fidelity as a function of χ/Ω. Here $N_\omega = 20$. Dashed (black) curves show $\exp[-\bar{n}\kappa k\pi/(2\chi)]$. Right: Fidelity as a function of the number of drive frequency components N_ω. Here $\chi/\Omega = 10$. Different symbols represent different amplitudes α as given in the legend.

transmon. The $\{|\mathcal{C}^+_\alpha\rangle, |\mathcal{C}^+_{i\alpha}\rangle\}$ encoding, which we shall call the memory encoding, is more convenient for autonomous quantum error correction [23]. This is due to the fact that both $|\mathcal{C}^+_\alpha\rangle$ and $|\mathcal{C}^+_{i\alpha}\rangle$ are eigenstates with eigenvalue $+1$ of the photon number parity operator $\mathbf{\Pi} = \exp(i\pi \boldsymbol{a}^\dagger \boldsymbol{a})$ and that the loss of a single-photon changes the photon number parity and can thus be detected by measuring $\mathbf{\Pi}$ [23,29]. In Sec. V, we provide a sequence of deterministic operations to switch between these two encodings and for the rest of this paper we focus on the computational encoding to discuss logical operations.

IV. SYNTHETIZING LOGICAL QUBIT OPERATIONS

We start by generalizing the conditional transmon rotation (8) by allowing for simultaneous driving of multiple photon number resolved resonances. Ideally this operation is given by

$$\boldsymbol{X}^{\mathcal{S}}_{\theta,\phi} = \sum_{n\in\mathcal{S}} |n\rangle\langle n| \otimes e^{i\frac{\theta}{2}\hat{n}_\phi\cdot\vec{\sigma}} + \sum_{m\notin\mathcal{S}} |m\rangle\langle m| \otimes \mathbb{1}, \qquad (12)$$

where $\mathcal{S} \subset \mathbb{N}$ denotes an arbitrary set of photon numbers. Such an operation can be approximately realized by the drive term (4) using a pulse of duration $T_p \gg \pi/(2\chi)$ with the following drive frequencies, component amplitudes, and phases

$$\nu_n = \omega_{eg} - 2n\chi, \quad \Omega_j = \delta_{jn}\frac{\theta}{T_p}, \quad \delta_j = \delta_{jn}\phi, \qquad (13)$$

where $n \in \mathcal{S}$. Imperfections will result from off-resonant driving of undesired photon number transitions as explained in more detail in Appendix A.

A central role in our Hadamard gate implementation is played by the odd photon number parity conditional π pulse given by (12) with $\theta = \pi$, $\phi = \pi/2$ and $\mathcal{S} = \{2n+1 : n \in \mathbb{N}\}$. Acting on the product state $|\alpha\rangle \otimes |g\rangle$, this gate ideally entangles the photon number parity with the state of the transmon as follows

$$\boldsymbol{X}^{\{2n+1:n\in\mathbb{N}\}}_{\pi,\frac{\pi}{2}} |\alpha\rangle \otimes |g\rangle = \frac{1}{\sqrt{2}}(|\mathcal{C}^+_\alpha\rangle|g\rangle + |\mathcal{C}^-_\alpha\rangle|e\rangle), \qquad (14)$$

where $|\mathcal{C}^-_\alpha\rangle = (|\alpha\rangle - |-\alpha\rangle)/\sqrt{2}$ is the odd parity cat state. Importantly, because the occupation probability of the Fock states in the coherent state $|\alpha\rangle$ obeys the Poisson distribution with mean $\bar{n} = |\alpha|^2$ and width $\sqrt{\bar{n}}$, it is sufficient to use a pulse with a finite number $N_\omega \gtrsim \sqrt{\bar{n}}$ of frequency components $\omega_n = \omega_{eg} - 2n\chi$, distributed around $\omega_{eg} - 2\bar{n}\chi$. Figure 2 shows the fidelity of the simulated entangling operation (14) as a function of the ratio χ/Ω (left) and as a function of N_ω (right) in the presence of photon loss. For square pulses, as used in the simulation, a simple pulse optimization consists in taking $\chi/\Omega = k \in \mathbb{N}$, since the spectral weight of the pulse with frequency component ω_n then vanishes identically at all other resonance frequencies $\omega_{m\neq n}$ (technically the zeros of the sinc function fall on the unwanted photon number resonances, as explained in Appendix A). As shown in the left panel of Fig. 2, the fidelity first increases with increasing k, which is due to the decreasing AC-Stark shift $\sim\Omega/k$ induced off resonance. However, increasing k also increases the duration of the π pulse $T_p = \pi/\Omega \sim k$ and hence increases the effect of photon loss, which leads to the observed decrease in fidelity. The dashed black curves on the left panel represent $\exp[-\bar{n}\kappa k\pi/(2\chi)]$ for the different coherent state amplitudes. On the right panel of Fig. 2 we observe the expected saturation of the fidelity when the number of frequency components becomes large compared with $\sqrt{\bar{n}}$. The parameters for the simulation are given in the figure caption. In Appendix A, we show that similar fidelities are obtained for Gaussian pulse envelopes. It is conceivable that more sophisticated pulse engineering could lead to further improvement.

A. A deterministic logical Hadamard gate

A deterministic Hadamard gate can be implemented by the following sequence of operations (to be read from right to left)

$$\boldsymbol{H}_L = \boldsymbol{D}_{\frac{\alpha}{2}}\boldsymbol{Y}^{\{2n+1:n\in\mathbb{N}\}}_{-\pi}\boldsymbol{D}_{\frac{\alpha}{2}}\boldsymbol{Y}^{0}_{-\pi}\mathbf{\Pi}^e\boldsymbol{D}^g_{-\alpha}\boldsymbol{Y}_{\frac{\pi}{2}}, \qquad (15)$$

where we have used the shorthand notation $\boldsymbol{Y}_\theta = \boldsymbol{X}_{\theta,\frac{\pi}{2}}$. The corresponding circuit diagram is shown in Appendix C.

The initial unconditional qubit rotation $\boldsymbol{Y}_{\frac{\pi}{2}}$ can be realized with a short pulse with center frequency $\omega_{eg} - \bar{n}\chi$ and duration $T_p \ll 1/(2\bar{n}\chi)$ such that its frequency spectrum approximately homogeneously covers a number of photon number resonances large compared with $\bar{n}$ [11]. Similarly, the unconditional cavity displacement $\boldsymbol{D}_{\frac{\alpha}{2}}$ can be realized by a pulse with center frequency ω_c and duration $T_p \ll 1/(2\chi)$ such that the cavity resonances corresponding to the ground and excited states of the transmon are equally driven [11].

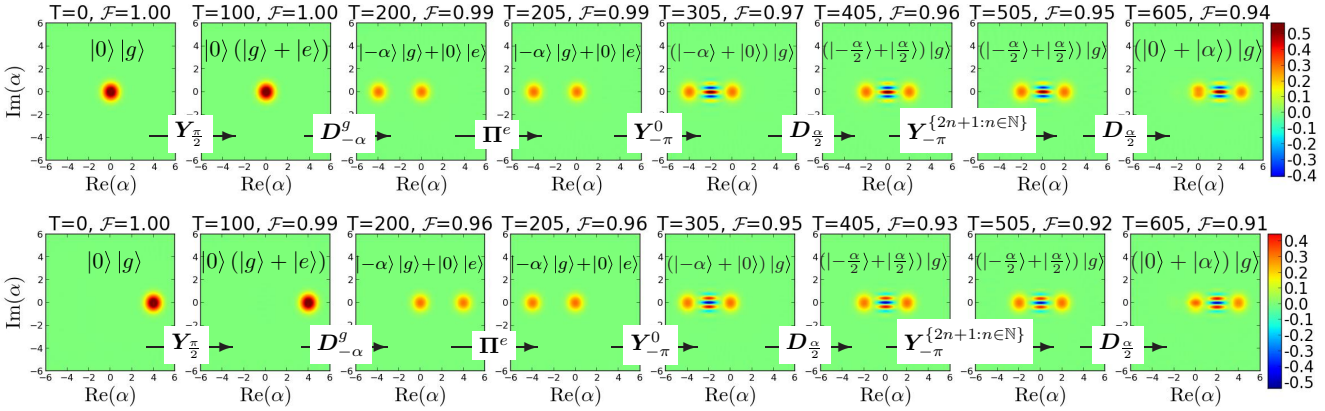

FIG. 3. (Color online) Wigner function $W(\alpha) = (2/\pi)\mathrm{tr}[\boldsymbol{\Pi}\boldsymbol{D}_{-\alpha}\rho_{\mathrm{cav}}\boldsymbol{D}_{\alpha}]$ of the reduced density matrix of the cavity after each operation in the Hadamard gate sequence (15). Top: for the initial state $|0\rangle_L$. Bottom: for the initial state $|1\rangle_L$. In this simulation we use $\alpha = 4$, $\chi/(2\pi) = 50\,\mathrm{MHz}$, and $\kappa = 10^{-4}\chi$ as well as square pulses with duration $T_p = 10\pi/\chi$ for both transmon rotations and field displacements. The fidelity $\mathcal{F}$ to the target state, which is indicated in each panel (omitting normalization) as well as the time T in ns are in shown in the title of each subfigure. Notice the phase difference of π in the interference fringes of the two final states.

As discussed in Appendix E, in order to avoid spurious population of higher transmon levels, it is however preferable to use more sophisticated pulse shaping in frequency. In the simulations we thus use longer square pulse envelopes ($T_p = 10\pi/\chi$) with narrow frequency bands around selected resonances for both conditional and unconditional operations. Clearly there is a tradeoff in minimizing the adverse effects of decoherence (increasing with pulse duration) and spurious transmon excitations (decreasing with pulse duration) and further optimization, beyond the scope of the present work, is desirable for an experimental realization. The results presented below, however, show that even with modest effort, rather high operation fidelities can be reached.

Figure 3 shows the Wigner function $W(\alpha) = (2/\pi)\mathrm{tr}[\boldsymbol{\Pi}\boldsymbol{D}_{-\alpha}\rho_{\mathrm{cav}}\boldsymbol{D}_{\alpha}]$ of the reduced density matrix of the cavity $\rho_{\mathrm{cav}} = \mathrm{tr}_{\mathrm{qb}}[\rho]$, where the full density matrix ρ is obtained by solving the master equation (6) following the sequence of operations (15), starting with the two computational basis states $|0\rangle_L$ (left) and $|1\rangle_L$ (right). The parameter values used are given in the figure caption. The fidelity of this Hadamard gate is defined as $\mathcal{F} = |\langle\psi_0|\boldsymbol{H}\langle g|\rho|g\rangle\boldsymbol{H}|\psi_0\rangle|^2$, where $\boldsymbol{H}$ is the ideal Hadamard transform. The fidelity depends on the initial state as shown in Fig. 4 where it is plotted as a function of the two angles θ and ϕ parametrizing the initial cavity state on the logical Bloch sphere as $|\psi_0\rangle = \cos(\theta/2)|0\rangle_L + e^{i\phi}\sin(\theta/2)|1\rangle_L$.

B. Phase gate via a conditional Berry phase

In order to achieve arbitrary single logical qubit rotations we next explain how to implement a phase gate or arbitrary rotation around the logical Z axis. Together with the above Hadamard gate, this gives the ability to perform arbitrary logical X rotations and therefore arbitrary logical single-qubit rotations. The phase gate is based on the concatenation property of displacement operations: $\boldsymbol{D}(\alpha)\boldsymbol{D}(\beta) = e^{(\alpha\beta^* - \alpha^*\beta)/2}\boldsymbol{D}(\alpha+\beta)$, which implies in particular the identity

$$\boldsymbol{D}^g_{\beta}\boldsymbol{D}^g_{-i\beta}\boldsymbol{D}^g_{-\beta}\boldsymbol{D}^g_{i\beta} = e^{2i\beta^2}|g\rangle\langle g| + \mathbb{1}|e\rangle\langle e|, \qquad (16)$$

where we took $\beta \in \mathbb{R}$. The phase $2\beta^2$ is in fact nothing else but the Berry phase [30] acquired by the coherent state upon undergoing a cyclic evolution along a closed path encircling an area β^2 in phase space. Thus by choosing $\beta = \sqrt{\theta/2}$, the following sequence (to be read from right to left) implements the desired phase gate

$$\boldsymbol{Y}^0_{\pi}\boldsymbol{D}^g_{\beta}\boldsymbol{D}^g_{-i\beta}\boldsymbol{D}^g_{-\beta}\boldsymbol{D}^g_{i\beta}\boldsymbol{Y}^0_{\pi} = e^{i\frac{\theta}{2}}e^{i\frac{\theta}{2}\boldsymbol{Z}_L}, \qquad (17)$$

where we have introduced $\boldsymbol{Z}_L = |1\rangle_L\langle 1| - |0\rangle_L\langle 0|$. Figure 5 shows the fidelity of this gate as a function of the angle θ for the initial state $|\psi\rangle_0 = (|0\rangle_L + |1\rangle_L)/\sqrt{2}$ for different values of α. In this simulation we fix the duration of the displacement operations. The nonmonotonic dependence of the fidelity on θ is due to the interplay between the photon-number-dependent decoherence rate and the θ-dependent variation of the photon number during the sequence (17).

C. Two qubit controlled phase gate

Two logical qubits may be coupled by dispersively coupling the fields of two adjacent cavities to a flux tunable split transmon as depicted in Fig. 6. Assuming that the inline transmon between cavities j and $j+1$ remains in its ground state

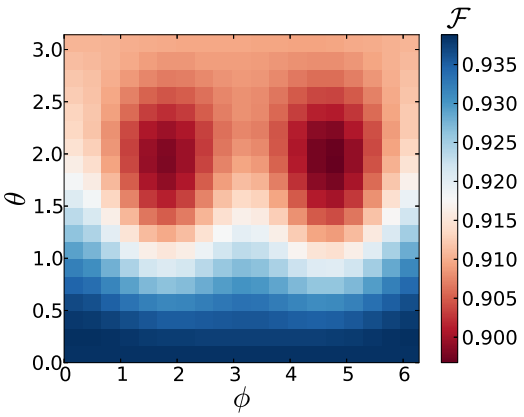

FIG. 4. (Color online) Fidelity of the deterministic Hadamard gate as a function of the initial cavity state parametrized on the logical Bloch sphere. Parameters used in the simulation are $\chi/(2\pi) = 50\,\mathrm{MHz}$, $\kappa = 10^{-4}\chi$, $\alpha = 4$, and square-pulse duration $T_p = 10\pi/\chi$. The total gate duration is $T_{\mathrm{tot}} = 6T_p + \pi/(2\chi) \approx 605\,\mathrm{ns}$.

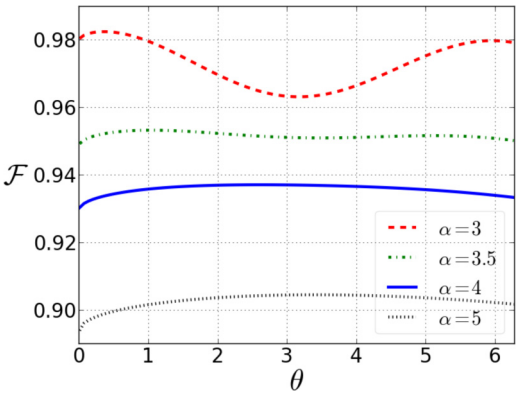

FIG. 5. (Color online) Fidelity of the phase gate as a function of θ for $\chi/(2\pi) = 50\,\mathrm{MHz}$, $\kappa = 10^{-4}\chi$ and fixed pulse duration $T_p = 10\pi/\chi$.

throughout, the dispersive interaction gives rise to a photon hopping term of the form $\xi_{jj+1}(\boldsymbol{a}_j^\dagger \boldsymbol{a}_{j+1} + \mathrm{H.c.})$. As shown in Ref. [6], such a term acting for a time T_p, naturally gives rise to a controlled phase gate $\mathbf{C}_\pi = |00\rangle\langle 00|_L + |01\rangle\langle 01|_L + |10\rangle\langle 10|_L - |11\rangle\langle 11|_L$ on the logical qubits (assumed to have equal amplitudes α in the state $|1\rangle_L$) provided that $\xi_{jj+1}T_p\bar{n} = \pi/2$ while $\bar{n} = |\alpha|^2 \gg \pi^2/4 \approx 2.5$. In this limit and for the dissipationless case, it can be shown that the worst case fidelity of this gate due to coherent state nonorthogonality goes as

$$\mathcal{F} \sim \exp\left(-\frac{\pi^2}{2\bar{n}}\right). \tag{18}$$

Since the linear decrease with $\bar{n}$ of the gate duration compensates the linear increase of the effective decoherence rate ($\gamma = \bar{n}\kappa$), it is obviously advantageous to use a large coherent state amplitude to increase the fidelity (18) of this gate. A suitably large amplitude can be obtained by preceding the controlled phase gate by the following amplitude pumping sequence on both cavities

$$\boldsymbol{Y}^0_{-\pi}\boldsymbol{D}^g_\beta\boldsymbol{Y}^0_\pi \tag{19}$$

with $\beta \in \mathbb{R}$ such that $\beta + \alpha > \alpha$. After the controlled phase gate the original amplitude can be restored by the following amplitude damping sequence on both cavities

$$\boldsymbol{Y}^0_{-\pi}\boldsymbol{D}^g_{-\beta}\boldsymbol{Y}^0_\pi. \tag{20}$$

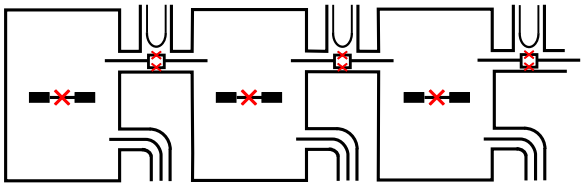

FIG. 6. (Color online) Chain of coupled 3D transmons. Crosses (red) represent the Josephson junctions at the center of each transmon. Each cavity is connected to its neighbors by an inline split transmon (SQUID loop). The cavities are represented by the rectangular boxes. The U-shaped lines between two cavities represents flux bias lines used to tune the transition frequencies of the inline transmons. A transmission line coupling to each cavity further allows for coherent microwave drives.

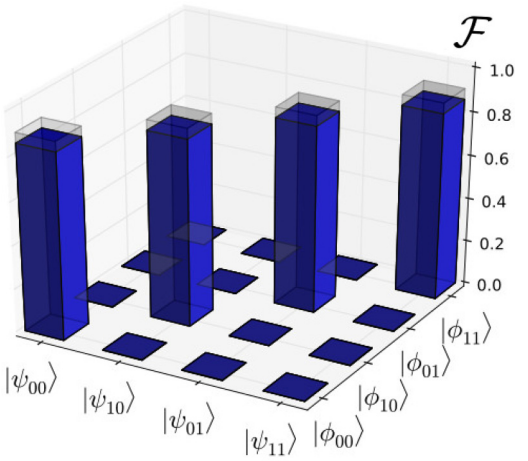

FIG. 7. (Color online) Controlled phase gate. The photon hopping strength is $\xi/(2\pi) = 25\,\mathrm{MHz}$ and the single-photon loss rate is $\kappa = 2 \times 10^{-4}\xi$. The solid bars show the results for $\alpha = 4$ and the semitransparent bars for $\alpha = 5$.

Figure 7 shows the matrix representation of the fidelity of the simulated controlled phase gate $\boldsymbol{C}_\pi$, acting on the $\boldsymbol{X}_L \otimes \boldsymbol{X}_L$ basis states $|\psi_{ij}\rangle = (|0\rangle_L + (-1)^i|1\rangle_L) \otimes (|0\rangle_L + (-1)^j|1\rangle_L)/2$, which are ideally mapped according to $|\psi_{ij}\rangle \to |\phi_{ij}\rangle$ onto the entangled states $|\phi_{ij}\rangle = (|00\rangle + (-1)^i|10\rangle + (-1)^j|01\rangle - (-1)^{i+j}|11\rangle)/2$. The fidelity is shown for two different values of α, demonstrating the increase in fidelity with increasing α. Parameter values used in the simulation are given in the figure caption.

Together with the single-qubit operations presented above, this completes the set of universal logic gates. A similar setup, albeit for a different two-qubit gate has been proposed in Ref. [12].

V. SWITCHING BETWEEN COMPUTATIONAL AND MEMORY ENCODINGS

In Mirrahimi *et al.* [12] a set of universal gates for logical qubits encoded in the memory basis (11) was given. An advantage of this proposal is that logical operations and quantum error correction take place within the same encoding, which allows for the logical operations to be made fault tolerant to a large extent [12]. One drawback of that specific proposal though, is that in order to implement an arbitrary single-qubit rotation in the memory encoding it is necessary to make use of the self-Kerr-interaction among the photons $-K\boldsymbol{a}^\dagger\boldsymbol{a}^\dagger\boldsymbol{a}\boldsymbol{a}$ (see Appendix D). The self-Kerr-interaction strength K is however typically orders of magnitude smaller than the dispersive interaction [20,31], leading to inappropriately long gate times. Increasing the strength of the self-Kerr-interaction is not desirable, since it adversely affects the logical state preparation, by squeezing the coherent states. As shown above, in the computational encoding (10), it is possible to implement deterministically an arbitrary single-qubit rotation using the cross-Kerr term between the photons and the transmon alone. Here we show that the cross-Kerr term also allows to switch between the two encodings. Thus a potentially faster mode of operation would consist in keeping the logical qubits in the protected memory encoding when idle, continuously

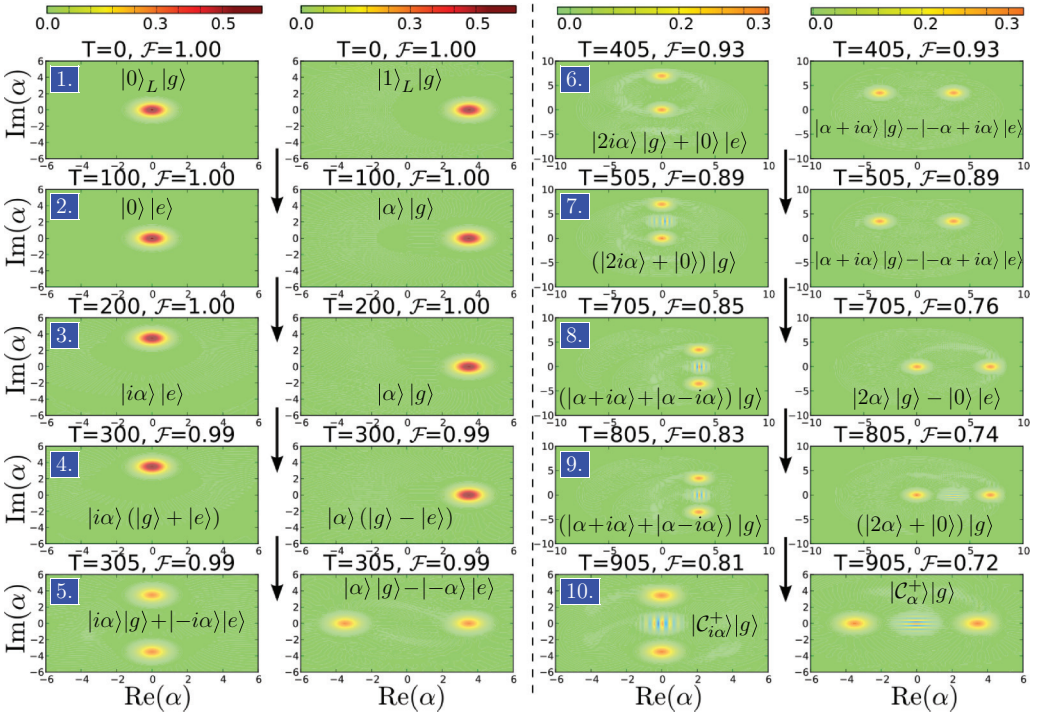

FIG. 8. (Color online) Evolution of the Wigner function of the two logical basis states $|0\rangle_L$ (first and third columns) and $|1\rangle_L$ (second and fourth columns) during the encoding-switching sequence (21). Here we take $\alpha = 3.5$, $\chi/(2\pi) = 50\,\mathrm{MHz}$, $\kappa = 10^{-4}\chi$, and varying pulse durations $T_p \in \{10\pi/\chi, 40\pi/\chi\}$. In each panel we indicate the ideal target state. The fidelity $\mathcal{F}$ of each step as well as the time T in ns is indicated in the titles.

performing error correction as described in Refs. [12,23] and map them into the computational encoding only to perform logic operations as described in the present work. The sequence of operations to switch from the computational to the memory encoding is given by

$$\boldsymbol{D}_{-\alpha}\boldsymbol{Y}^0_{\pi}\boldsymbol{D}_{\alpha}\boldsymbol{D}_{-i\alpha}\boldsymbol{Y}^0_{-\pi}\boldsymbol{D}_{i\alpha}\boldsymbol{\Pi}^e\boldsymbol{Y}_{-\frac{\pi}{2}}\boldsymbol{D}^e_{i\alpha}\boldsymbol{Y}^0_{\pi}. \tag{21}$$

The inverse transformation is obtained by inverting the sequence and replacing $\alpha \to -\alpha$ as well as $\pi \to -\pi$. Figure 8 shows the evolution of the Wigner function of the logical qubit basis states after each operation in the sequence (21). In order to shorten the duration of the sequence we have combined the two successive displacements using $\boldsymbol{D}_{\alpha}\boldsymbol{D}_{-i\alpha} = e^{i\alpha^2}\boldsymbol{D}_{\alpha-i\alpha}$. We find fidelities of 81% and 72% for the transformations $|0\rangle_L \to |\mathcal{C}^+_{i\alpha}\rangle$ and $|1\rangle_L \to |\mathcal{C}^+_{\alpha}\rangle$ respectively.

VI. SUMMARY AND CONCLUSION

In summary we have proposed a deterministic Hadamard gate for logical coherent state qubits encoded in the two-dimensional space spanned by the vacuum and a coherent state of finite amplitude. Our scheme utilizes the experimentally demonstrated strong dispersive interaction of the electromagnetic field of a superconducting cavity with an off-resonant effective two-level system (transmon qubit) and generalizes a recently introduced set of conditional operations [11]. We further describe a set of universal deterministic quantum gates and provide numerical estimates for fidelities that should be achievable in state of the art circuit QED systems.

ACKNOWLEDGMENT

This work was supported financially by the Swiss National Science Foundation.

APPENDIX A: APPENDIX A: PHOTON-NUMBER SUBSET CONDITIONAL TRANSMON ROTATION

In this Appendix we describe in more details how to implement operation (12). In a frame rotating with the bare transmon and cavity frequencies, a photon number subset S-dependent transmon pulse is described by the Hamiltonian

$$\boldsymbol{H} = -\chi\boldsymbol{a}^\dagger\boldsymbol{a}\boldsymbol{\sigma}^z + \sum_{m\in S}\frac{\Omega_m(t)}{2}(e^{-2im\chi t}\boldsymbol{\sigma}^- + \mathrm{H.c.}) \tag{A1}$$

where $\Omega_m(t)$ is the envelope function of the pulse component with center frequency $\omega_m = \omega_{eg} - 2m\chi$. Moving to the interaction picture with the unitary transformation

$$\boldsymbol{U}(t) = \exp\left[-it\chi\boldsymbol{\sigma}^z\sum_n n\,|n\rangle\,\langle n|\right] \tag{A2}$$

we obtain

$$\begin{aligned}\tilde{\boldsymbol{H}} &= \boldsymbol{U}\boldsymbol{H}\boldsymbol{U}^\dagger - i\boldsymbol{U}\dot{\boldsymbol{U}}^\dagger = \sum_{m\in S}\frac{\Omega_m}{2}\sum_n(e^{-2i\chi t(m-n)}\boldsymbol{\sigma}^- + \mathrm{H.c.})\,|n\rangle\,\langle n| \\ &= \sum_{m\in S}\frac{\Omega_m}{2}\boldsymbol{\sigma}^x\,|m\rangle\,\langle m| + \sum_{m\in S}\frac{\Omega_m}{2}\sum_{n\neq m}(e^{-2i\chi t(m-n)}\boldsymbol{\sigma}^- + \mathrm{H.c.})\,|n\rangle\,\langle n|\,.\end{aligned} \tag{A3}$$

Consider now the perturbative expansion for $\Omega_m/\chi \ll 1$ of the evolution operator in this frame

$$\begin{aligned}\boldsymbol{U}_{\rm evol}(T) &= \mathcal{T}\exp\left[-i\int_0^T \tilde{\boldsymbol{H}}(\tau)d\tau\right] \approx 1 - i\int_0^T \tilde{\boldsymbol{H}}(\tau)d\tau \\ &= 1 - \frac{i}{2}\sum_{m\in S}\left\{\int_0^T d\tau\,\Omega_m(\tau)\boldsymbol{\sigma}^x\,|m\rangle\langle m| + \sum_{\underline{n}\neq m}\int_0^T d\tau\,\frac{\Omega_m(\tau)}{2}(e^{-2i\chi(m-n)\tau}\boldsymbol{\sigma}^- + \text{H.c.})\,|n\rangle\langle n|\right\}. \qquad \text{(A4)}\end{aligned}$$

For $\Omega_m(\tau) = \theta(T-\tau)\Omega_0$ this becomes

$$\boldsymbol{U}_{\rm evol}(T) \approx 1 - i\frac{\Omega_0 T}{2}\sum_{m\in S}\left[\boldsymbol{\sigma}^x\,|m\rangle\langle m|\sum_{\underline{n}\neq m} e^{-i\chi(m-n)T}\left(\frac{\sin(\chi(m-n)T)}{\chi(m-n)T}\boldsymbol{\sigma}^- + \text{H.c.}\right)|n\rangle\langle n|\right]. \qquad \text{(A5)}$$

Now let us choose T such that $\chi T = \pi$. Then the second term above vanishes identically, as the zeros of the sine function line up with the photon resonances of the transmon that we do not wish to drive and we have

$$\boldsymbol{U}_{\rm evol}(\pi/\chi) \approx 1 - i\pi\left(\frac{\Omega_0}{2\chi}\right)\sum_{m\in S}\boldsymbol{\sigma}^x\,|m\rangle\langle m|. \qquad \text{(A6)}$$

This generates a small x rotation of the transmon components associated with the Fock states $|m\rangle$ with $m \in S$ by an angle $\pi\Omega_0/\chi \ll \pi$. By concatenating such rotations k times, effectively increasing the total pulse time to $T = k\pi/\chi$, we can then generate a rotation of the transmon by an angle $k\pi\Omega_0/\chi$ as

$$\begin{aligned}\boldsymbol{U}_{\rm evol}(k\pi/\chi) &\approx \boldsymbol{U}_{\rm evol}(\pi/\chi)^k \\ &= \exp\left[-i\frac{k\pi\Omega_0}{2\chi}\boldsymbol{\sigma}^x\right]\sum_{m\in S}|m\rangle\langle m| \\ &\quad + \sum_{n\notin S}|n\rangle\langle n|. \qquad \text{(A7)}\end{aligned}$$

By changing the phase of the drive signal we may similarly implement a photon parity conditional rotation around arbitrary axes in the x-y plane. For example we may perform a π rotation around the y axis conditioned on the parity of the photon number being odd as in the main text by selecting a drive phase of π, $S = \{2n+1\}_{n\in\mathbb{N}}$ and $k\Omega_0 = \chi$, which implies $k \gg 1$ given that we assumed $\Omega_0 \ll \chi$. Higher-order terms in the perturbative expansion (A4), lead to correction terms of order Ω_0^2/χ, which correspond to the AC-stark shift [20].

In reality one cannot generate perfect square pulses and this will lead to corrections. It is easily seen that for Gaussian pulse envelopes, the strength of the residual on-resonance drives of other resonances is suppressed at least by the superexponential factor $\sum_{k=1}^{\infty} e^{-(2\chi T k)^2}$ and thus becomes negligible for a pulse duration $T \gg 1/(2\chi)$. Note also that typically for a conditional qubit rotation by an angle $\theta \in [0,2\pi]$, $T \sim \theta/\Omega_0$, which means the correction terms will be small as long as $\Omega_0 \ll \chi$ consistent with our assumption. Figure 9 shows the fidelity of the odd photon number parity conditional π pulse implemented with Gaussian pulses $A_\pi \exp\{-[\sigma(t-T/2)]^2/2\}$ with frequency width $\sigma = 6/T$, total pulse duration $T_p = 10\pi/\chi$ and amplitude $A_\pi = \pi\sigma/\sqrt{2\pi}$. The comparison with the square pulse case, shows that similar fidelities can be reached in both cases.

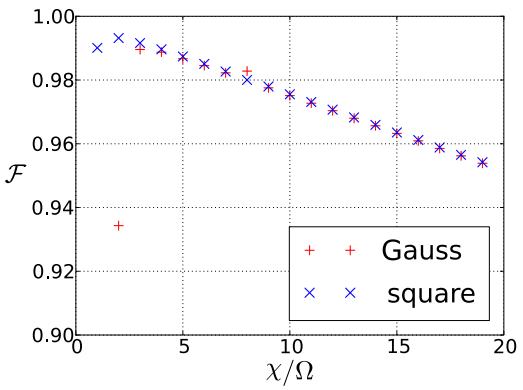

FIG. 9. (Color online) Comparison of the fidelities of the photon number parity conditional π pulse between Gaussian and square pulses. For small χ/Ω, the fidelity is lower for the Gaussian pulses, which is due to the larger on-resonance driving of unwanted transitions in this case. For larger χ/Ω, the obtained fidelities are similar. We take $\alpha = 4$, $N_\omega = 20$, $\chi/(2\pi) = 50$ MHz, and $\kappa = 10^{-4}\chi$.

APPENDIX B: NOT GATE

Although one may in principle implement any single-qubit gate with the operations described in the main text, the dispersive coupling may allow for more efficient direct implementations of certain gates. For example, a logical quantum NOT gate $\boldsymbol{X}_L$ can be implemented solely with unconditional operations by the sequence of operations

$$\boldsymbol{X}_L = \boldsymbol{D}_{\frac{\alpha}{2}}\boldsymbol{Y}_\pi\boldsymbol{\Pi}^e\boldsymbol{Y}_\pi\boldsymbol{D}_{-\frac{\alpha}{2}}. \qquad \text{(B1)}$$

APPENDIX C: CIRCUIT DIAGRAM OF THE DETERMINISTIC HADAMARD GATE

Logical qubit operations may be conveniently represented as quantum circuits. Figure 10 shows the circuit diagram of the deterministic logical Hadamard gate.

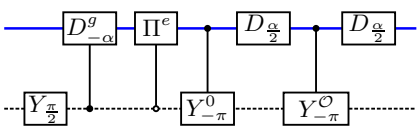

FIG. 10. (Color online) Circuit diagram for the deterministic Hadamard gate. The horizontal solid (blue) line represents the cavity state (logical qubit), while the dashed (black) line represents the transmon state. Here $\mathcal{O} = \{2n+1 : n \in \mathbb{N}\}$.

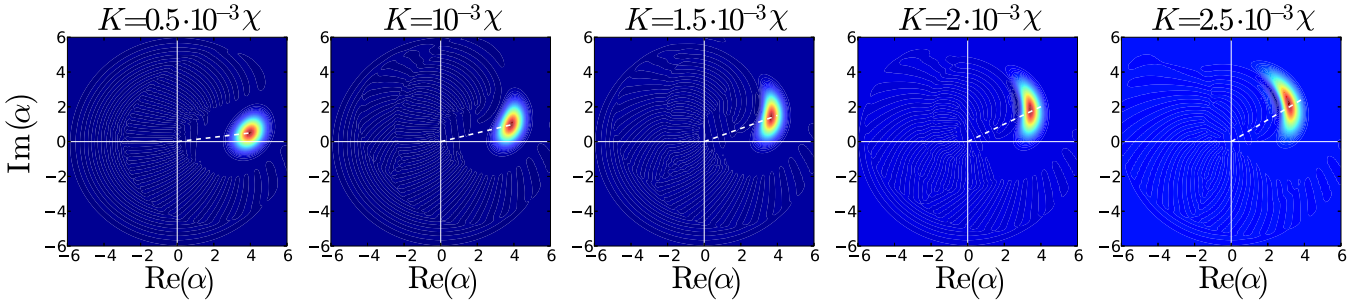

FIG. 11. (Color online) Effect of the self-Kerr-interaction on the displacement operation. The displacement amplitude is $\alpha = 4$ and the square pulse duration is $T_p = 10\pi/\chi$. We further take $\chi/(2\pi) = 50\,\mathrm{MHz}$ and $\kappa = 0$. The initial state is $|0\rangle_L\,|g\rangle$ and the Wigner function is calculated by solving numerically the master equation (6) with Hamiltonian $\boldsymbol{H} = i\varepsilon(\boldsymbol{a} - \boldsymbol{a}^\dagger) - K\boldsymbol{a}^\dagger\boldsymbol{a}^\dagger\boldsymbol{a}\boldsymbol{a}$. The dashed (white) lines show $a(T_p)$ after Eq. (D6).

APPENDIX D: INFLUENCE OF THE INDUCED PHOTON-PHOTON INTERACTION

In the above discussion we have neglected the self-Kerr-interaction between the photons induced by the coupling to the nonlinear transmon oscillator [31–33]. In this Appendix, we show that the leading-order effect of the self-Kerr can be accounted and corrected for to a large extent. The self-Kerr effect is described by the term

$$\boldsymbol{H}_K = -K\boldsymbol{a}^\dagger\boldsymbol{a}^\dagger\boldsymbol{a}\boldsymbol{a}. \tag{D1}$$

Note that this term commutes with the photon number operator and is independent of the state of the transmon and thus commutes with the conditional transmon operations (8) and (12). When acting on a coherent state $|\alpha\rangle$ the leading-order effect is a phase rotation [34]

$$e^{-i\boldsymbol{H}_K t}\,|\alpha\rangle \approx |\alpha e^{i\phi_K t}\rangle \qquad Kt \ll 1 \tag{D2}$$

with $\phi_K = 2\bar{n}K$. Sub-leading-order terms describe squeezing [34]. To leading order, the effect of the self-Kerr on the photon number parity operation (9) can thus be corrected for simply by shortening the waiting time according to

$$T_{\pi,\bar{n}} = \frac{\pi}{2(\chi + K\bar{n})}, \tag{D3}$$

for a coherent state with average photon number $\bar{n}$. The self-Kerr term (D1) does not commute with the displacement operation (7). Let us consider the case where the transmon is in the ground state. In the presence of an on-resonance drive with constant strength $\varepsilon \in \mathbb{R}$ and of duration T such that $KT \ll 1$, the Heisenberg equation of motion for the annihilation operator, neglecting squeezing terms reads

$$\dot{\boldsymbol{a}}(t) = 2iK(\varepsilon t)^2\boldsymbol{a} + \varepsilon. \tag{D4}$$

The solution of Eq. (D4) for the coherent state amplitude is

$$a(t) = \left(\varepsilon\int_0^t d\tau e^{-i\frac{2}{3}K\varepsilon^2\tau^3} + a(0)\right)e^{i\frac{2}{3}K\varepsilon^2 t^3}. \tag{D5}$$

Specifically for the case where the field is initially the vacuum $[a(0) = 0]$ and for $(\varepsilon t)^2 Kt \ll 1$ we find

$$a(t) \approx \varepsilon t + i\frac{K\varepsilon^3 t^4}{2}. \tag{D6}$$

The self-Kerr induced phase rotation during the displacement is thus

$$\phi_K(t) \approx \tan\phi_K = \frac{\mathrm{Im}[a(t)]}{\mathrm{Re}[a(t)]} = \frac{K\bar{n}(t)t}{2}, \tag{D7}$$

where we have defined $\bar{n}(t) = (\varepsilon t)^2$. Figure 11 compares Eq. (D6) for different values of K with the result of a Wigner function computation including higher-order terms. As we can see, the direction of the center of the distribution is well captured by (D6) (dashed white lines) even in the presence of sizable squeezing. To emphasize the effect of the self-Kerr we set $\kappa = 0$ in this simulation.

Figure 12 shows the cavity Wigner function during the Hadamard gate sequence acting on the initial state $(|0\rangle_L + |1\rangle_L)/\sqrt{2}$, including a self-Kerr term of strength $K = 0.5 \times 10^{-4}\chi$. Here we include photon loss as well. In the simulation we have adjusted the displacement phases and amplitudes according to Eq. (D6) and corrected the wait time according to Eq. (D3). The results demonstrate that high fidelities of about

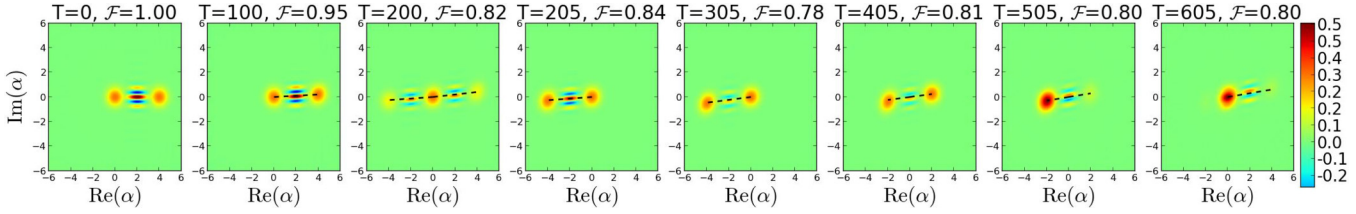

FIG. 12. (Color online) Effect of the self-Kerr-interaction on the Hadamard gate. We use a displacement of amplitude $\alpha = 4$ and pulse duration $T_p = 10\pi/\chi$ and take $\chi/(2\pi) = 50\,\mathrm{MHz}$ and $\kappa = 10^{-4}\chi$. The initial state is $(|0\rangle_L + |1\rangle_L)/\sqrt{2}$ and the Wigner function is calculated by solving numerically the master equation (6) including the self-Kerr term (D1) with $K = 0.5 \times 10^{-4}\chi$. The fidelity $\mathcal{F}$ as well as the time T in ns at each step are shown in the titles. The (black) dashed lines are calculated analytically.

80% can be reached even in the presence of a weak self-Kerr term.

APPENDIX E: BEYOND THE TWO LEVEL APPROXIMATION: CONDITIONAL VS UNCONDITIONAL OPERATIONS

Above, we have neglected the higher excited states of the transmon. However, a transmon is best viewed as a weakly anharmonic oscillator with negative anharmonicity [18,33]. Denoting the transmon eigenstates with $|j\rangle$, the dispersive Hamiltonian in the multilevel case reads

$$\sum_{j=0} \chi_{j,j+1}(|j+1\rangle\langle j+1| - |j\rangle\langle j|)\boldsymbol{a}^\dagger \boldsymbol{a}. \tag{E1}$$

Thus the $e \leftrightarrow g$ and $f \leftrightarrow e$ transitions split up into photon-number-resolved ladders of resonances according to

$$\omega_n^{(eg)} = \omega_{eg} - 2n\chi \tag{E2}$$

and

$$\omega_n^{(fe)} = \omega_{fe} - 2n\chi' \tag{E3}$$

with $\chi = \chi_{01} - \chi_{12}/2$ and $\chi' = \chi_{12} - (\chi_{23} + \chi_{01})/2$.

If the magnitude δ of the anharmonicity were much larger than $2\bar{n}\chi$ where $\bar{n}$ is the average photon number in the logical qubit state $|1\rangle_L$, then one could implement unconditional operations on the transmon simply by using pulses of short duration T such that $\delta \gg 1/T \gg 2\bar{n}\chi$. If such a wide separation of frequency scales is not available, as is the case in current experimental realizations, then it may be preferable to implement the unconditional operations in a similar way to the conditional operations, by superposing narrow frequency band pulses to avoid spurious population of higher transmon levels (see Fig. 13). The penalty for this is an increase in gate duration.

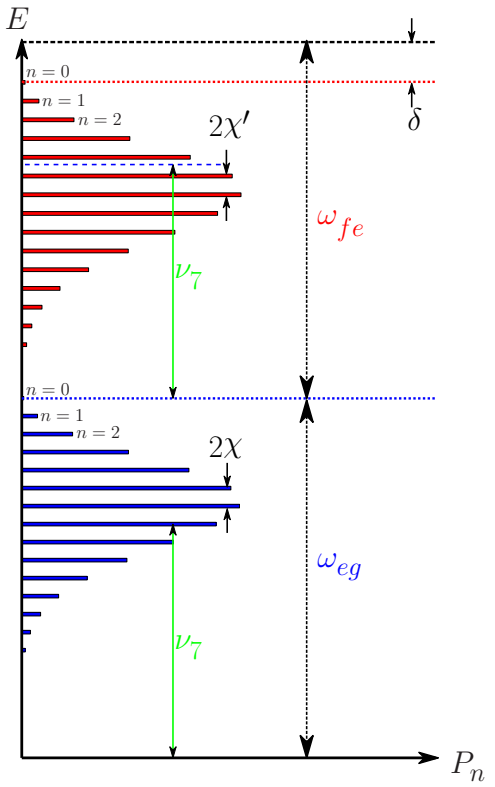

FIG. 13. (Color online) Illustration of the three-level transmon spectrum in the dispersive coupling regime with a coherent state in the cavity. Note that $\chi \neq \chi'$. Thus, by using sufficiently narrow pulse envelopes in frequency, one can avoid population of the excited state f. This is illustrated on the figure for the $n = 7$ transition.

[1] S. Lloyd and S. L. Braunstein, Phys. Rev. Lett. **82**, 1784 (1999).
[2] D. Gottesman, A. Kitaev, and J. Preskill, Phys. Rev. A **64**, 012310 (2001).
[3] H. Paik, D. I. Schuster, L. S. Bishop, G. Kirchmair, G. Catelani, A. P. Sears, B. R. Johnson, M. J. Reagor, L. Frunzio, L. I. Glazman, S. M. Girvin, M. H. Devoret, and R. J. Schoelkopf, Phys. Rev. Lett. **107**, 240501 (2011).
[4] C. Rigetti, J. M. Gambetta, S. Poletto, B. L. T. Plourde, J. M. Chow, A. D. Córcoles, J. A. Smolin, S. T. Merkel, J. R. Rozen, G. A. Keefe, M. B. Rothwell, M. B. Ketchen, and M. Steffen, Phys. Rev. B **86**, 100506 (2012).
[5] R. W. Andrews, R. W. Peterson, T. P. Purdy, K. Cicak, R. W. Simmonds, C. A. Regal, and K. W. Lehnert, arXiv:1310.5276.
[6] T. C. Ralph, A. Gilchrist, G. J. Milburn, W. J. Munro, and S. Glancy, Phys. Rev. A **68**, 042319 (2003).
[7] C. M. Savage, S. L. Braunstein, and D. F. Walls, Opt. Lett. **15**, 628 (1990).
[8] M. Brune, S. Haroche, J. M. Raimond, L. Davidovich, and N. Zagury, Phys. Rev. A **45**, 5193 (1992).
[9] S. Deléglise, I. Dotsenko, C. Sayrin, J. Bernu, M. Brune, J.-M. Raimond, and S. Haroche, Nature (London) **455**, 510 (2008).
[10] E. Schroedinger, Naturwissenschaften **23**, 807 (1935).
[11] Z. Leghtas, G. Kirchmair, B. Vlastakis, M. H. Devoret, R. J. Schoelkopf, and M. Mirrahimi, Phys. Rev. A **87**, 042315 (2013).
[12] M. Mirrahimi, Z. Leghtas, V. V. Albert, S. Touzard, R. J. Schoelkopf, L. Jiang, and M. H. Devoret, arXiv:1312.2017.
[13] H. Jeong and M. S. Kim, Phys. Rev. A **65**, 042305 (2002).
[14] P. Marek and J. Fiurasek, Phys. Rev. A **82**, 014304 (2010).
[15] A. P. Lund, T. C. Ralph, and H. L. Haselgrove, Phys. Rev. Lett. **100**, 030503 (2008).
[16] A. Tipsmark, R. Dong, A. Laghaout, P. Marek, M. Jezek, and U. L. Andersen, Phys. Rev. A **84**, 050301 (2011).
[17] A. Blais, R.-S. Huang, A. Wallraff, S. M. Girvin, and R. J. Schoelkopf, Phys. Rev. A **69**, 062320 (2004).
[18] J. Koch, T. M. Yu, J. Gambetta, A. A. Houck, D. I. Schuster, J. Majer, A. Blais, M. H. Devoret, S. M. Girvin, and R. J. Schoelkopf, Phys. Rev. A **76**, 042319 (2007).
[19] D. I. Schuster, A. A. Houck, J. A. Schreier, A. Wallraff, J. M. Gambetta, A. Blais, L. Frunzio1, J. Majer, B. Johnson, M. H. Devoret, S. M. Girvin, and R. J. Schoelkopf, Nature (London) **445**, 515 (2007).

[20] B. Vlastakis, G. Kirchmair, Z. Leghtas, S. E. Nigg, L. Frunzio, S. M. Girvin, M. Mirrahimi, M. H. Devoret, and R. J. Schoelkopf, Science **342**, 607 (2013).
[21] The Lamb shift is implicitly absorbed into a renormalization of the cavity and qubit transition frequencies.
[22] J. Johansson, P. Nation, and F. Nori, Comput. Phys. Comm. **183**, 1760 (2012).
[23] Z. Leghtas, G. Kirchmair, B. Vlastakis, R. J. Schoelkopf, M. H. Devoret, and M. Mirrahimi, Phys. Rev. Lett. **111**, 120501 (2013).
[24] A. Gilchrist, K. Nemoto, W. J. Munro, T. C. Ralph, S. Glancy, S. L. Braunstein, and G. J. Milburn, J. Opt. B: Quantum Semiclass. Opt. **6**, S828 (2004).
[25] M. J. Everitt, T. P. Spiller, G. J. Milburn, R. D. Wilson, and A. M. Zagoskin, arXiv:1212.4795.
[26] S. Haroche and J.-M. Raimond, *Exploring the Quantum, Atoms, Cavities and Photons* (Oxford Graduate Texts, Oxford, 2006).
[27] M. O. Scully and W. E. Lamb, Phys. Rev. **179**, 368 (1969).
[28] H. Wang, M. Hofheinz, M. Ansmann, R. C. Bialczak, E. Lucero, M. Neeley, A. D. O'Connell, D. Sank, J. Wenner, A. N. Cleland, and J. M. Martinis, Phys. Rev. Lett. **101**, 240401 (2008).
[29] L. Sun, A. Petrenko, Z. Leghtas, B. Vlastakis, G. Kirchmair, K. M. Sliwa, A. Narla, M. Hatridge, S. Shankar, J. Blumoff, L. Frunzio, M. Mirrahimi, M. H. Devoret, and R. J. Schoelkopf, arXiv:1311.2534.
[30] Note that for a harmonic oscillator the adiabaticity condition is always satisfied.
[31] G. Kirchmair, B. Vlastakis, Z. Leghtas, S. E. Nigg, H. Paik, E. Ginossar, M. Mirrahimi, L. Frunzio, S. M. Girvin, and R. J. Schoelkopf, Nature (London) **495**, 205 (2013).
[32] J. Bourassa, F. Beaudoin, J. M. Gambetta, and A. Blais, Phys. Rev. A **86**, 013814 (2012).
[33] S. E. Nigg, H. Paik, B. Vlastakis, G. Kirchmair, S. Shankar, L. Frunzio, M. H. Devoret, R. J. Schoelkopf, and S. M. Girvin, Phys. Rev. Lett. **108**, 240502 (2012).
[34] D. F. Walls and G. J. Milburn, *Quantum Optics*, 2nd ed. (Springer, Berlin, 2008).